Heliyon 10 (2024) e24496

Contents lists available at ScienceDirect

Heliyon

journal homepage: www.cell.com/heliyon

Research article

Novel phosphor GdY_2SbO_7 co-dope with Eu^{3+} and Bi^{3+} for optical thermometer

Yanru Yin, Mengmeng Jiang, Lianhua Tian *

Department of Physics, Yanbian University, Yanji, 133002, China

ARTICLE INFO

Keywords:
Fluorescence intensity ratio
Thermally coupled levels
Optical thermometry

ABSTRACT

A series of GdY_2SbO_7:Bi^{3+}, Eu^{3+} phosphors were prepared using the conventional solid-state reaction. In this study, the photoluminescence properties and temperature sensitivity of the samples were investigated. When Bi^{3+} and Eu^{3+} were codoped into GdY_2SbO_7, the intensity of Bi^{3+} decreased with increasing Eu^{3+} concentration, indicating a potential energy transfer from Bi^{3+} to Eu^{3+}. To examine the temperature sensitivity of the sample, its emission spectrum was investigated in the range of 300–500 K. Based on different temperature dependences of Bi^{3+} and Eu^{3+}, the relative sensitivity (S_r) and absolute sensitivity (S_a) of the samples were calculated using the fluorescence intensity ratio (FIR) and thermochromic methods. In FIR modes, S_r based on I^{3+}_{Eu}/I^{3+}_{Bi} reached 1.26 % K^{-1} at 500 K, while S_r on double excitation method reached 1.36 % K^{-1} at 340 K. In addition, according to the thermochromic properties of GdY_2SbO_7:Bi^{3+}, Eu^{3+} phosphor, the temperature-sensing ability of the sample was investigated, and S_r reached a maximum value of 0.5996 % K^{-1} at 300 K.

1. Introduction

Temperature is a crucial physical parameter in numerous industrial operations and scientific research. Because of their accuracy, sensitivity, and applicability to complex environments, non-contact fluorescence thermometers have attracted considerable research interest in recent years and are used for temperature measurements in medicine, chemistry, and other industries [1,2]. Two main temperature measurement strategies are generally practiced: one is temperature measurement using a pair of thermally coupled levels (TCL), where the relative sensitivity (S_r) is directly proportional to the energy gap of the relevant TCLs [3]. The second is based on the fluorescence intensity ratio (FIR) of the dual luminescence center. The FIR temperature-sensing material usually exhibits two or more distinct emission peaks as the monitoring signals, using which the temperature can be calibrated by analyzing the variation of the ratio of emission peak integral intensity with the varying temperatures of samples [4]. For the TCL mode, lanthanide elements with rich energy levels are widely used to implement this strategy [5,6]. However, owing to the small gap (200–2000 cm^{-1}) between the thermally coupled levels, the relative sensitivity of this mode to the sample is limited [7]. Therefore, in this study, we used dual-activated luminescence temperature probes to modify and improve sensitivity [8]. The FIR mode has received considerable attention because its relative sensitivity is not limited by the energy level gap. Several studies have been reported on dual-mode optical thermometers, such as $SrMgAl_{10}O_7$:Mn^{2+}/Mn^{4+} [9], $NaZr_2(PO_4)_3$:Eu^{2+}/Eu^{3+} [10], and $YNbO_4$:Pr^{3+}/Tb^{3+} [11].

Because the principle of the dual luminescence center temperature measurement mode is based on the thermal quenching effect of

* Corresponding author.
E-mail address: lhtian@ybu.edu.cn (L. Tian).

https://doi.org/10.1016/j.heliyon.2024.e24496
Received 10 August 2023; Received in revised form 21 December 2023; Accepted 10 January 2024
Available online 20 January 2024

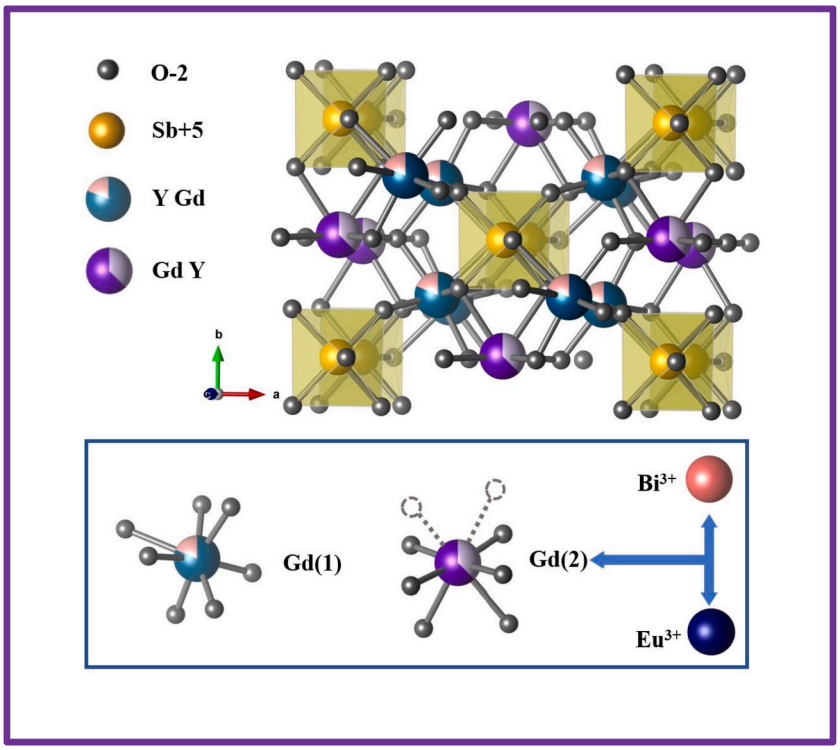

Fig. 1. Crystal structure diagram of GYSO host and coordination environment of Gd, Y, and Sb cations in the lattice.

ion fluorescence [12]. The exploitation of the emissions of Bi^{3+} and single trivalent rare earth (Re^{3+}) ions can perform the temperature measurement, because they have completely different electronic structures. The fluorescence intensity of Bi^{3+} is readily affected by the environment because of its naked 6s electrons, whereas the Re^{3+} ions are less affected by temperature due to the outer electronic configuration of $5s^25p^6$ [13,14]. On the other hand, Bi^{3+} ions were used as sensitizer co-doped with Re^{3+} in some host materials due to the energy transfer from Bi^{3+} to Re^{3+} ions. Several studies have been reported such as $LaVO_4$:Bi^{3+}/Eu^{3+} [15], LaNbO4:Bi^{3+}/Ln^{3+} (Ln = Eu/Tb/Dy/Sm) [14] and $Ca_3Sc_2Si_3O_{12}$:Bi^{3+}/Tb^{3+}/Eu^{3+} [16]. Among them, the exploitation of the emissions of $Bi^{3+}$and Eu^{3+} ions are a facile approach to achieve higher efficient energy transfer. Meanwhile, the fluorescence emission spectrum of Eu^{3+} hardly overlaps with that of Bi^{3+}. Therefore, phosphors codoped with Bi^{3+} and Eu^{3+} are excellent temperature-sensing materials [17–22]. In addition, antimonates are often used as fluorescent material substrates because of their chemical stability and low synthesis costs [3, 23,24]. To the best of our knowledge, GdY_2SbO_7 has not been reported as a phosphor host. Therefore, in the current study, GdY_2SbO_7 was chosen as the host material for phosphors.

Herein, $Gd_{0.99\text{-}y}Y_2SbO_7$:0.01$Bi^{3+}$, y$Eu^{3+}$ (y = 0.01, 0.05, 0.10, 0.15, 0.20, 0.25, and 0.30) phosphors were prepared using conventional solid-state reactions. The crystal structure and luminescence properties of the phosphors, along with their temperature-dependent sensing properties, were investigated. The absolute and relative sensitivities of the phosphor samples were calculated in FIR and thermochromic methods, respectively. Two kinds of FIR methods were adopted in our works. One was FIR based on I_{Eu}^{3+}/I_{Bi}^{3+}, the other was on double excitation method. Our findings revealed that Bi^{3+}/Eu^{3+} codoped phosphors exhibit energy transfer, outstanding thermal properties, and excellent temperature sensitivity. The details of the study are discussed in the following sections.

2. Experimental

A series of phosphor samples, $Gd_{0.99-y}Y_2SbO_7$:0.01Bi^{3+}, yEu^{3+} (y = 0.01, 0.05, 0.10, 0.15, 0.20, 0.25, and 0.30), were prepared using conventional solid-state reactions. The raw materials were high-purity Gd_2O_3 (99.99 %, Aladdin), Y_2O_3 (99.99 %, Aladdin), Sb_2O_3 (99.99 %, Aladdin), Eu_2O_3 (99.99 %, Aladdin), and Bi_2O_3 (99.99 %, Aladdin), weighed according to the stoichiometric ratio. All raw materials were ground in an agate mortar for 30 min, then loaded into a crucible, placed in a muffle furnace, and sintered at 1350 °C for 40 h, respectively. After the phosphor had naturally cooled to room temperature, the sample was ground again for subsequent testing.

To analyze the crystal structure of the samples, X-ray diffraction (XRD) patterns were recorded using a powder diffractometer (D/max-2200/PC, Rigaku, Japan) with Cu Kα radiation (λ = 1.5406 Å) in the 2θ range of 10°–90°. Scanning electron microscopy (SEM), energy dispersive spectroscopy, and the element distribution maps were measured using a field-emission scanning electron microscope (SU-8010, Hitachi, Japan). The F-7000 spectrometer (Hitachi, Japan) and 450 W xenon lamp were used to test the photoluminescence

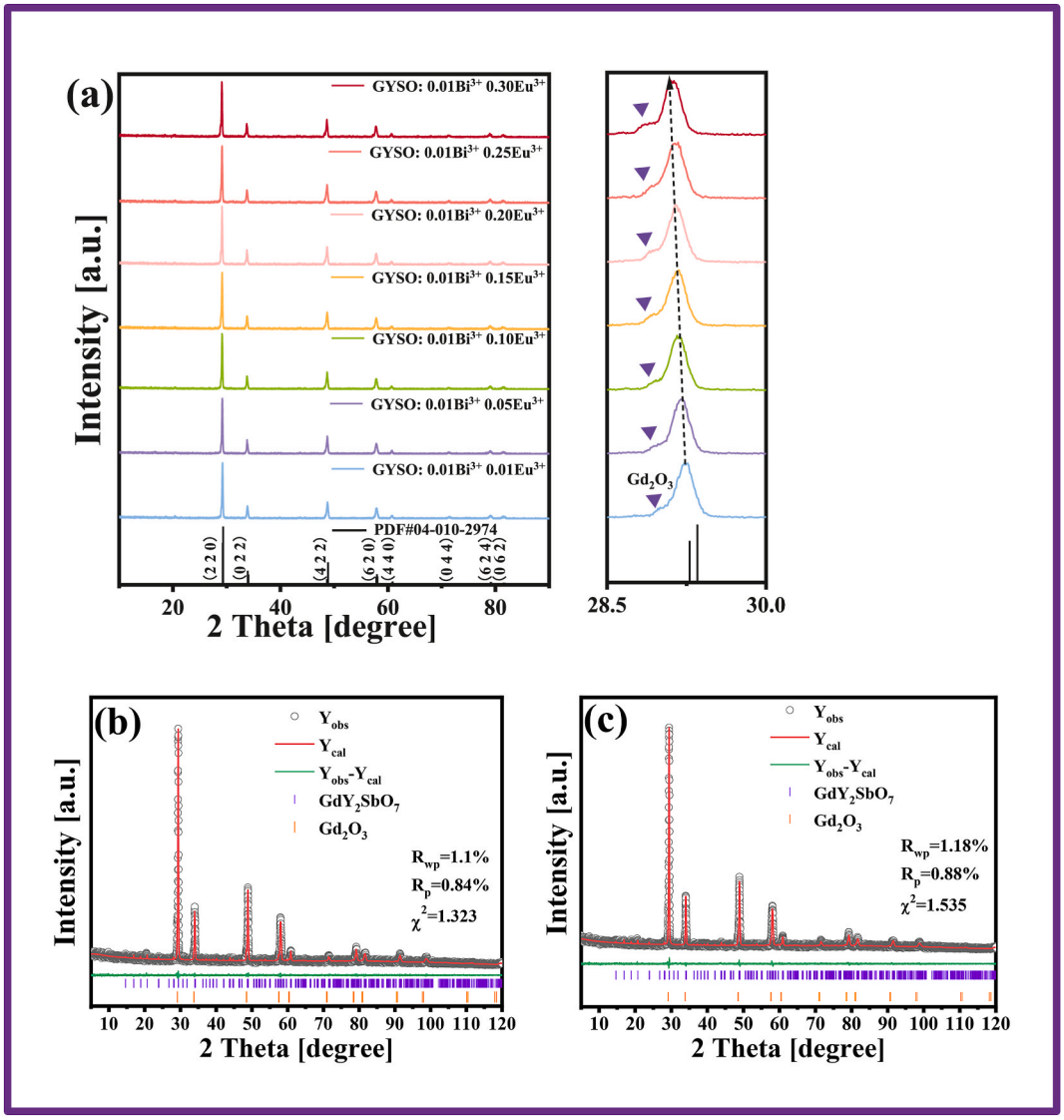

Fig. 2. (a) X-ray diffraction spectra of $G_{0.99-y}YSO:0.01Bi^{3+}$, yEu^{3+}(y = 0.01, 0.05, 0.10, 0.15, 0.20, 0.25, and 0.30) and standard GYSO data (PDF#04–010–2974). The inset shows a magnified XRD pattern in the range of 28–31°. The Rietveld refinement of (b) GYSO and (c) $GYSO:0.01Bi^{3+}/0.15Eu^{3+}$.

and photoluminescence excitation spectra. The aforementioned experiments were performed at room temperature. The decay curves and temperature-dependent luminescence spectra were obtained using an FLS-980 spectrometer (Edinburgh Instruments, England).

3. Results and discussion

The crystal structure of the GYSO host is shown in Fig. 1. GYSO exhibits an orthogonal structure with space group $C222_1$. The crystal parameters are $a = 10.5172$ Å, $b = 7.4527$ Å, $c = 7.4806$ Å, and $V = 586.3409$ Å^3. In this structure, Gd^{3+} and Y^{3+} occupy two types of sites: the 4b site with an eight coordination and the 8c site with a seven coordination. The presence of six oxygen ions and two vacant anion sites around the ion at the Gd (2) position leads to the octa coordination of Gd^{3+} at this position. The six-coordinated Sb ions are staggered with the eight-coordinated Gd (2) position ions, forming planes parallel to the a direction, and between these planes are arranged the seven-coordinated Gd (1) position ions. In the phosphor samples, Bi^{3+} (r = 1.17 Å, CN = 8) and Eu^{3+} (r = 1.066 Å, CN = 8) replaced ions at position Gd (2) (r = 1.053 Å, CN = 8) owing to the similar ionic radii and following the Judd–Ofelt theory [25].

The XRD patterns of the synthesized $Gd_{0.99-y}Y_2SbO_7:0.01Bi^{3+}$, yEu^{3+} (y = 0.01, 0.05, 0.10, 0.15, 0.20, 0.25, and 0.30) phosphors are displayed in Fig. 2. It can be seen that the most diffraction peaks of the samples match the GYSO standard card (PDF#04-010-2974) considerably well. Apart from this, the small amounts of Gd_2O_3 impurity were detected in the samples. However, the luminescence of

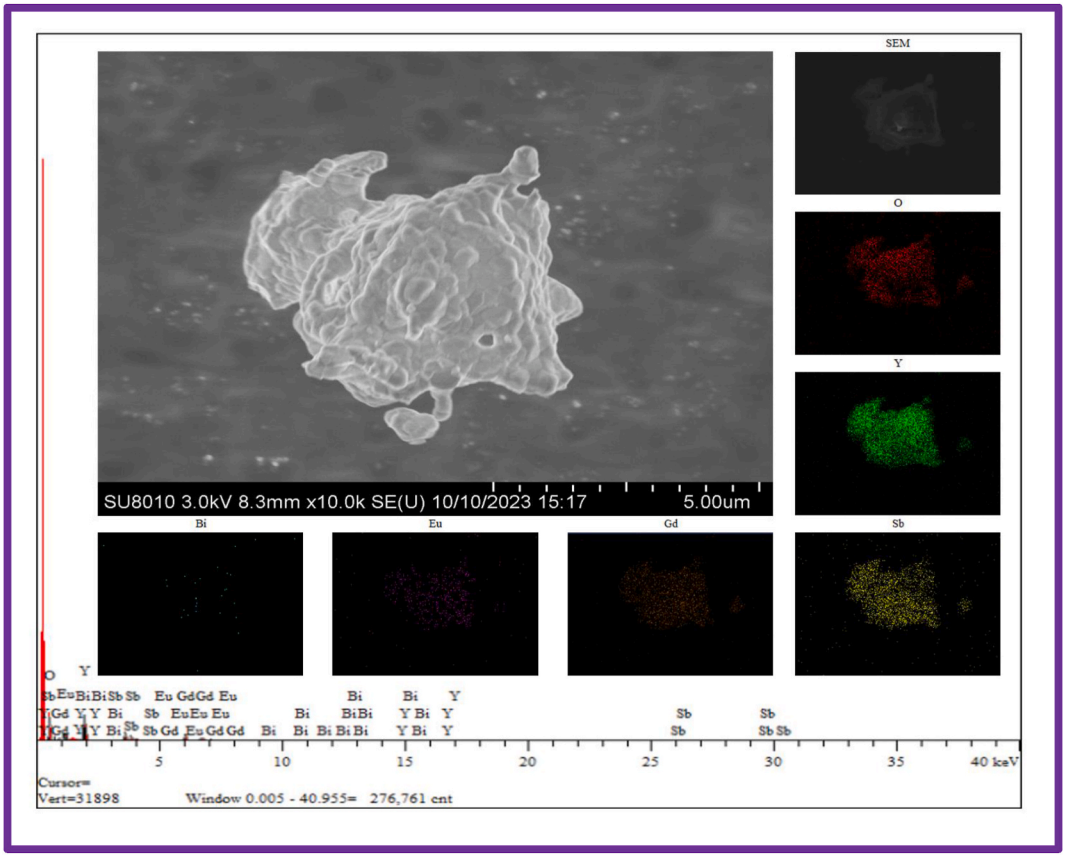

Fig. 3. SEM image and EDS pattern of GYSO:0.01Bi^{3+}/0.15Eu^{3+}.

impurity is too weak to influence the luminescence characteristics of GYSO:Bi^{3+},Eu^{3+}. The inset shows a magnified XRD pattern in the range of 28°–31°. The slight shift of the diffraction peaks indicates that Eu^{3+} and Bi^{3+} were successfully doped into the hosts. As shown in Fig. 2(b) and (c), the XRD data of GYSO and GYSO:0.01Bi^{3+}/0.15Eu^{3+} phosphors were refined by the Rietveld method using the GSAS software. The refinement results showed that the values of R_{wp}, R_p, and χ^2 were 1.1 %, 0.84 %, 1.323 and 1.18 %, 0.88 %, 1.535, respectively. It indicated that the refinement results are reasonable and reliable.

The SEM image of GYSO:0.01Bi^{3+}/0.15Eu^{3+} is shown in Fig. 3, which indicates that the sample comprises irregular particles with a size of approximately 0.3 μm. The elemental mapping result shows that Gd, Y, Sb, Eu, and Bi are uniformly distributed throughout the range of phosphor particles.

Fig. 4 (a) shows the excitation spectrum of GYSO:0.15Eu^{3+} monitored at 580 nm. The spectrum comprises two parts. The broadband absorption centered at 274 nm is attributed to the $O^{2-} \rightarrow Eu^{3+}$ charge transfer. The subsequent weak absorption peak at 393 nm corresponds to the $^7F_0 \rightarrow {}^5L_6$ transition of Eu^{3+} [18,19]. Fig. 4 (b) shows the PL of G_{1-x}YSO:xEu^{3+} (x = 0.01, 0.05, 0.10, 0.15, and 0.20) samples. Under the excitation wavelength of 274 nm, a series of emission peaks appear in the range of 580–713 nm, owing to the $^5D_0 \rightarrow {}^7F_{0,1,2,3,4}$ transition of Eu^{3+} [26–29]. In the current host, Gd^{3+} contains two types of sites: the 4b site with eight coordination and the 8c site with seven coordination. According to the Judd–Ofelt theory, the emission caused by the $^5D_0 \rightarrow {}^7F_2$ electric dipole transition dominates when Eu^{3+} occupies the noncentrosymmetric site. However, the $^5D_0 \rightarrow {}^7F_1$ magnetic dipole transition dominates when Eu^{3+} occupies the centrosymmetric site. The fluorescence emission of Eu^{3+} at 587 nm ($^5D_0 \rightarrow {}^7F_1$) is stronger than that at 627 nm ($^5D_0 \rightarrow {}^7F_2$), as shown in Fig. 4 (b), which proves that Eu^{3+} is more likely to occupy the Gd (2) centrosymmetric site with the eight coordination [30,31]. As the concentration of Eu^{3+} increases, the emission intensity of the host (446 nm) becomes weaker, while that of Eu^{3+} becomes stronger, indicating the possibility of energy transfer from the host to Eu^{3+} [32]. The emission intensity of Eu^{3+} is strongest at x = 0.15 and then decreases because of the concentration quenching effect.

The excitation and emission spectra of GYSO:0.01Bi^{3+}, GYSO:0.15Eu^{3+}, and GYSO:0.01Bi^{3+}/0.15Eu^{3+} are shown in Fig. 5. Under 301 nm excitation, GYSO:0.01Bi^{3+} shows a broad emission band in the 350–500 nm range with the maximum at 426 nm, corresponding to the $^1S_0 \rightarrow {}^3P_1$ transition of Bi^{3+}, as shown in Fig. 5 (a). As monitored at 426 nm, the obtained excitation spectrum shows two bands. One of broad absorption band is at 270–350 nm originating from the Bi^{3+} transition ($^1S_0 \rightarrow {}^3P_1$) and the other located at about 250 nm belongs to ($^1S_0 \rightarrow {}^1P_1$) transition [33]. To illustrate the possibility of energy transfer between Bi^{3+} and Eu^{3+}, the inset of

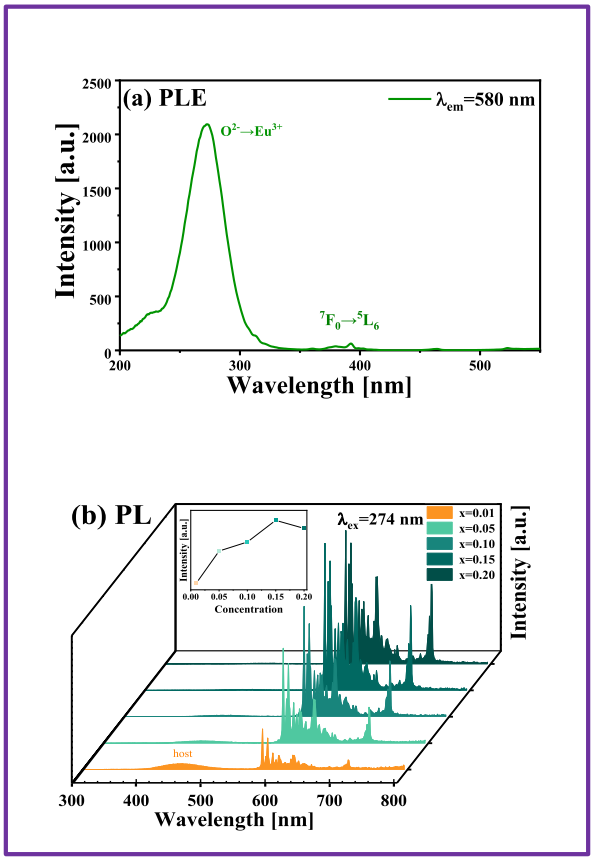

Fig. 4. (a) PLE spectrum of GYSO:0.15Eu^{3+} phosphor. (b) The PL spectra of a series of $G_{1-x}YSO:xEu^{3+}$ (x = 0.01, 0.05, 0.10, 0.15, and 0.20). The inset shows the variation of the maximum value of fluorescence intensity of the samples with Eu^{3+} concentration.

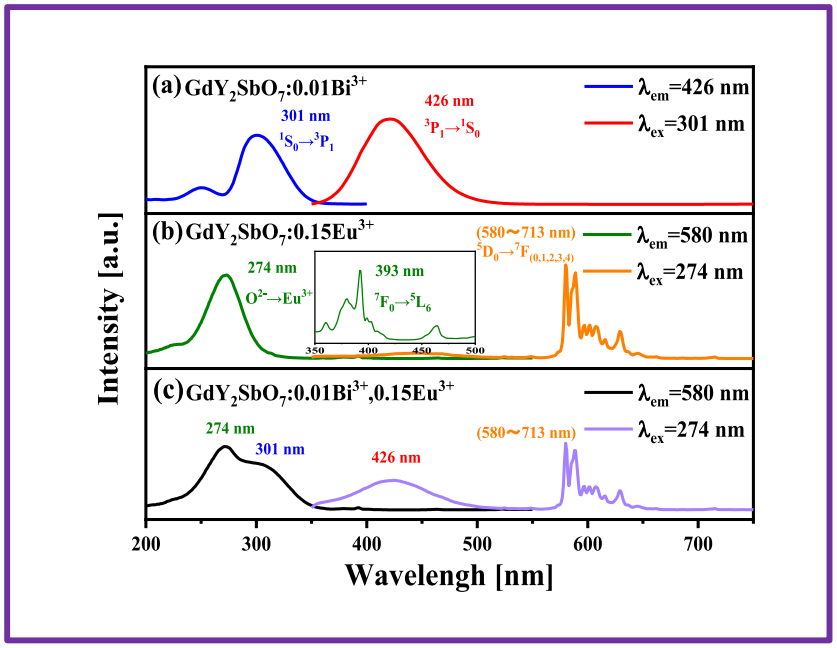

Fig. 5. PL and PLE spectra at room temperature of (a) GYSO: 0.01Bi^{3+}, (b) GYSO: 0.15Eu^{3+}, and (c) GYSO: 0.01Bi^{3+}/0.15Eu^{3+}. The inset shows the PLE spectrum of GYSO: 0.15Eu^{3+} in the 350 nm–500 nm range magnified in the vertical coordinate.

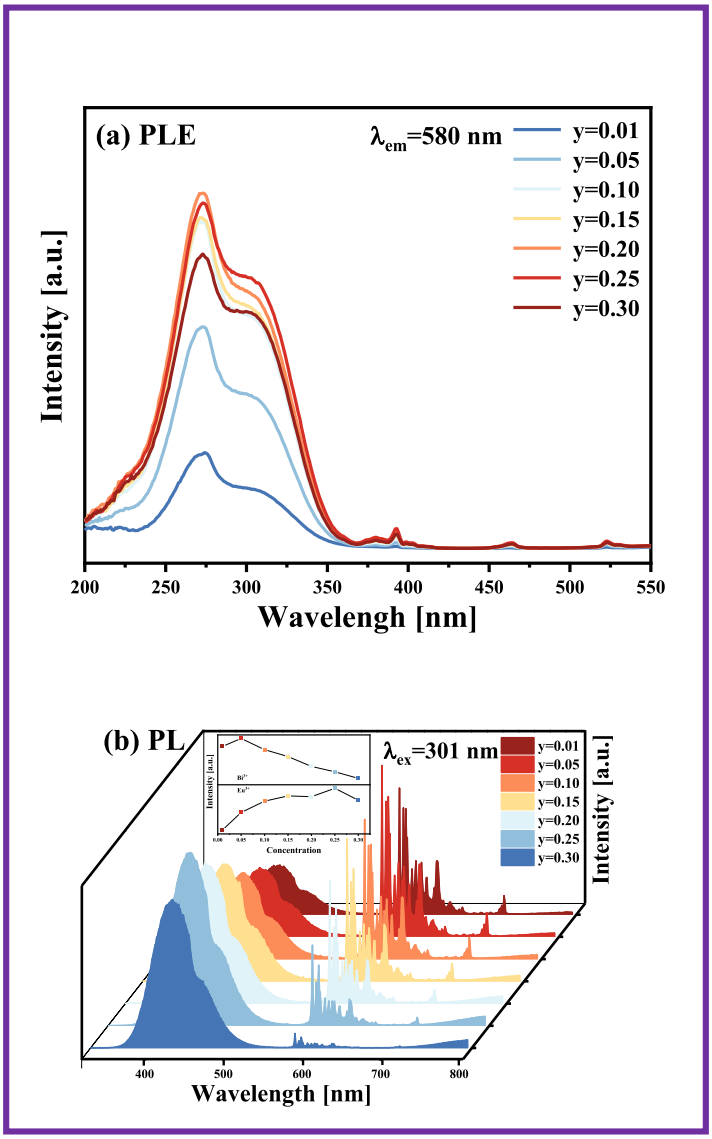

Fig. 6. PL and PLE spectra of $G_{0.99\text{-}y}YSO:0.01Bi^{3+}$, yEu^{3+} (y = 0.01, 0.05, 0.10, 0.15, 0.20, 0.25, and 0.30). The inset shows the variation of the maximum value of fluorescence intensity of Bi^{3+} and Eu^{3+} with the concentration of Eu^{3+}.

Fig. 5 (b) shows an image of the excitation spectrum with magnified vertical coordinates in the range of 350–500 nm. The emission spectrum of $GYSO:0.01Bi^{3+}$ overlaps with the excitation spectrum of $GYSO:0.15Eu^{3+}$, indicating a probable energy transfer occurring between Eu^{3+} and Bi^{3+}. For optical thermometer applications, we investigated the photoluminescence properties of Bi^{3+}/Eu^{3+} that were codoped into the GdY_2SbO_7 phosphors. As shown in Fig. 5 (c), the absorption bands of $GYSO:0.01Bi^{3}/0.15Eu^{3+}$ primarily comprise Bi^{3+} ion $^1S_0 \rightarrow {}^3P_1$ (~301 nm) transition and $O^{2-} \rightarrow Eu^{3+}$ charge transfer (274 nm) under 580 nm monitoring. The emission peaks of the codoped samples comprise Bi^{3+} ion $^1S_0 \rightarrow {}^3P_1$ (426 nm) and Eu^{3+} ion $^5D_0 \rightarrow {}^7F_{0,1,2,3,4}$ (580–713 nm) transitions ($\lambda_{ex} = 301$ nm) [34].

The excitation and photoluminescence spectra of $G_{0.99-y}YSO:0.01Bi^{3+}$, yEu^{3+} (y = 0.01, 0.05, 0.10, 0.15, 0.20, 0.25, and 0.30) are shown in Fig. 6 (a) and (b), respectively. The shape of the excitation spectra of the samples did not change considerably. When the concentration of Eu^{3+} was less than 0.2, the intensity of the emission band of Bi^{3+} decreased, while that of Eu^{3+} increased with increasing Eu^{3+} concentration. This indicates an energy transfer from Bi^{3+} to Eu^{3+}. The intensity of the Eu^{3+} emission band decreased when the Eu^{3+} concentration was continuously increased, owing to the concentration quenching effect.

To further prove the energy transfer, the lifetime decay curves of $G_{0.99\text{-}y}YSO:0.01Bi^{3+}$, yEu^{3+} (y = 0.05, 0.10, 0.15, 0.20, 0.25, and 0.30) monitored at 420 nm were measured and described in Fig. 7. The attenuation curve fits a double exponential equation (1) well

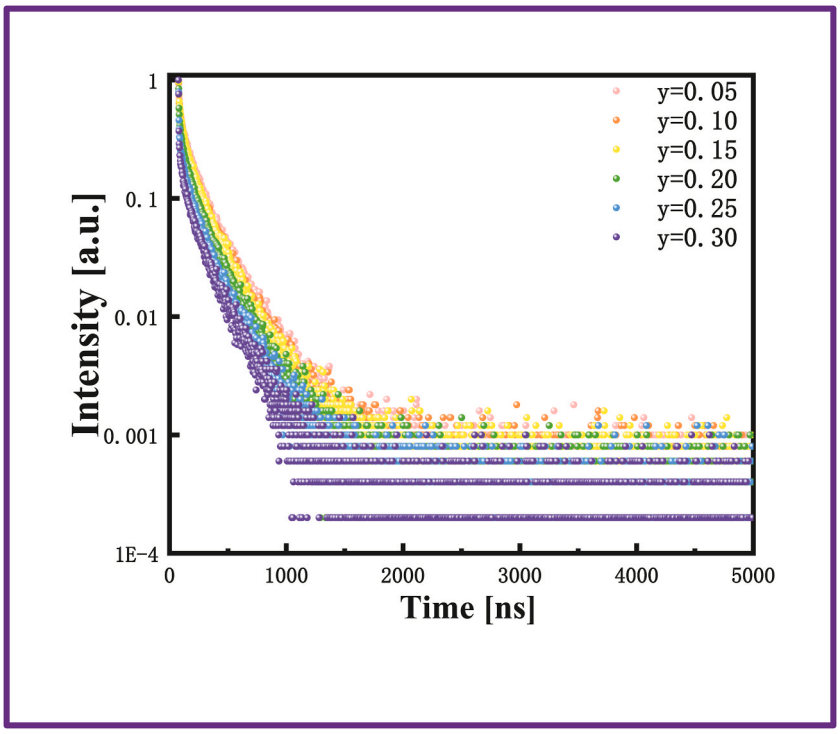

Fig. 7. Decay curves of Bi^{3+} in $G_{0.99\text{-}y}YSO:0.01Bi^{3+}$, yEu^{3+} (y = 0.05, 0.10, 0.15, 0.20, 0.25, and 0.30).

[33]:

$$I(t) = A_1 \exp\left(-\frac{t}{\tau_1}\right) + A_2 \exp\left(\frac{t}{\tau_2}\right) + I_0, \tag{1}$$

where I(t) represents the emission intensity, τ_1 and τ_2 are defined as decay times, and A_1, A_2, and I_0 are fitting constants. The following equation (2) is used to calculate the average decay time [33]:

$$\bar{\tau} = \frac{A_1\tau_1{}^2 + A_2\tau_2{}^2}{A_1\tau_1 + A_2\tau_2}. \tag{2}$$

The average lifetimes of Bi^{3+} in $G_{0.99-y}YSO:0.01Bi^{3+}$, yEu^{3+} (y = 0.05, 0.10, 0.15, 0.20, 0.25, and 0.30) phosphors are 15.867, 12.998, 11.992, 6.630, 4.940, and 4.173 ns, respectively. When the concentration of Eu^{3+} increases, the fluorescence lifetime of Bi^{3+} progressively decreases. This further proves that an energy transfer occurs from Bi^{3+} to Eu^{3+}.

To determine the temperature sensitivity of the samples, the temperature dependence of $GYSO:0.01Bi^{3+}$, $0.05Eu^{3+}$ was studied in the range of 300–500 K with 274 and 301 nm as the excitation wavelengths respectively as shown in Fig. 8 (a) and (b), respectively. The lattice vibration of the host strongly depend on the temperature of the phosphor. Therefore at higher temperature, the enhanced lattice vibration would cause the intense nonradiative transition processes which is usually characterized by the decrease in luminescence intensity [35,36]. Besides, due to the different electronic configuration of Bi^{3+} and Eu^{3+} ions, Bi^{3+} ions are more susceptible to the influence of surrounding environment than Eu^{3+} ions. Moreover, the probability of energy transfer from Bi^{3+} to Eu^{3+} increases with the rise of the temperature. It results the luminescence intensities of Bi^{3+} and Eu^{3+} are decreased by different degrees with rising the temperature. Therefore, the emission peaks of Bi^{3+} and Eu^{3+} can be selected for non-contact fluorescence temperature measurement.

According to the intensity histogram shown in Fig. 9, the fluorescence intensities of Bi^{3+} and Eu^{3+} do not change remarkably in the range of 300–340 K. However, when the temperature is higher than 340 K, the luminescence decreases considerably and the quenching of Bi^{3+} is faster than that of Eu^{3+}. Based on this phenomenon shown in Fig. 10 (a) and (b), the FIR of Eu^{3+} and Bi^{3+} can be used as a temperature measurement parameter. FIR with these two ions is expressed by the following equation (3) [18]:

$$FIR = \frac{I_{Eu^{3+}}(T)}{I_{Bi^{3+}}(T)} = \frac{I_{Eu^{3+}}}{I_{Bi^{3+}}} \frac{1 + A_{Eu^{3+}} \exp\left(-\frac{E_{Eu^{3+}}}{k_B T}\right)}{1 + A_{Bi^{3+}} \exp\left(-\frac{E_{Bi^{3+}}}{k_B T}\right)} \approx C + B \exp\left(-\frac{\Delta E}{k_B T}\right), \tag{3}$$

where C and B are constants, ΔE is the thermal quenching activation energy, k_B is the Boltzmann constant, and T is the temperature.

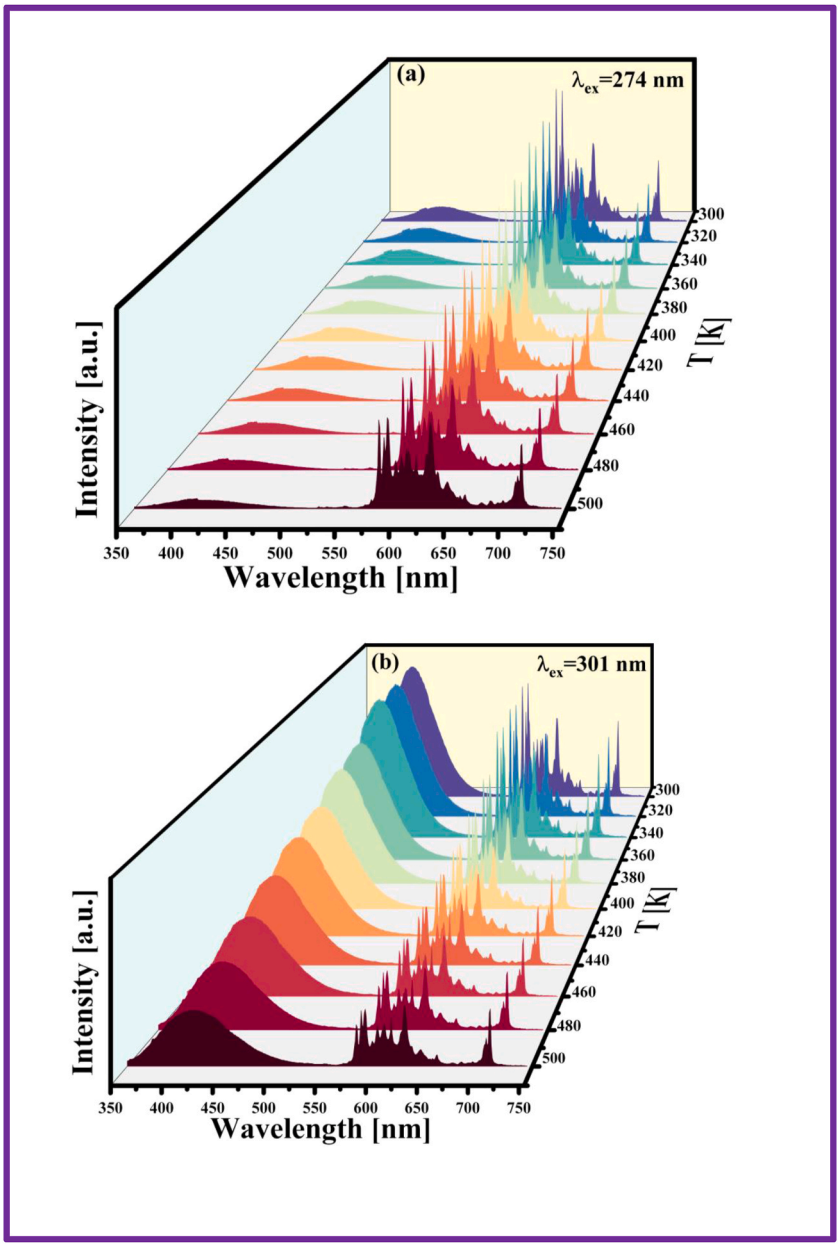

Fig. 8. Temperature-dependent photoluminescence spectra of GYSO:0.01Bi^{3+}, 0.05Eu^{3+} at 300–500 K with the excitation wavelengths of (a) 274 nm (b) 301 nm.

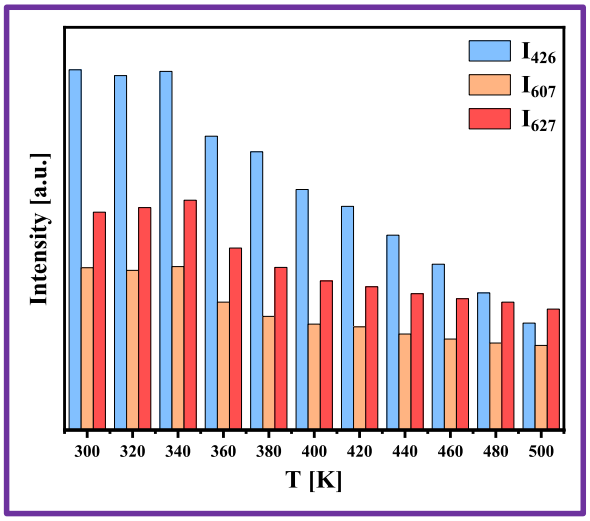

Fig. 9. Histogram of the intensity of Bi^{3+} and Eu^{3+} at varying temperatures under 301 nm excitation.

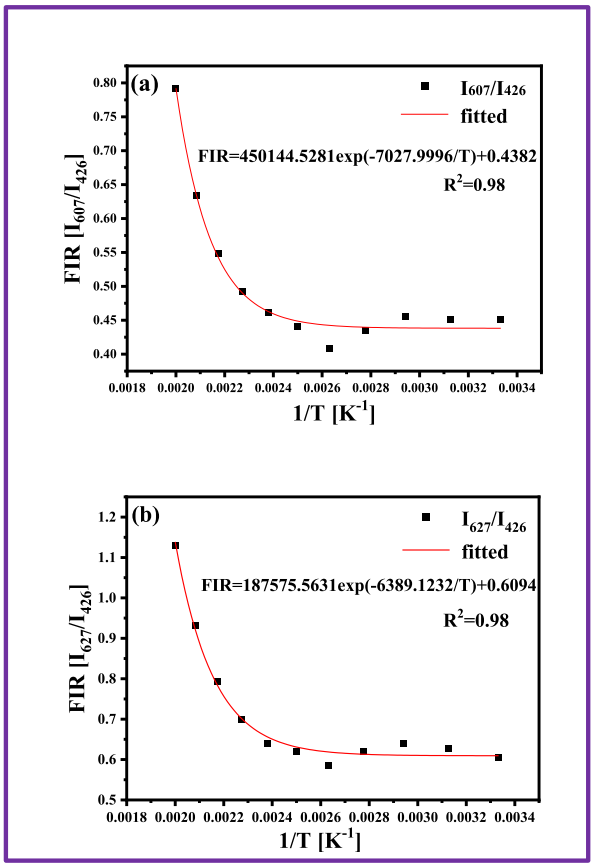

Fig. 10. The fitting curves of $FIR(I_{607}/I_{426})$ (a) and $FIR(I_{627}/I_{426})$ (b) on temperature for GYSO:0.01Bi^{3+}, 0.05Eu^{3+} phosphor.

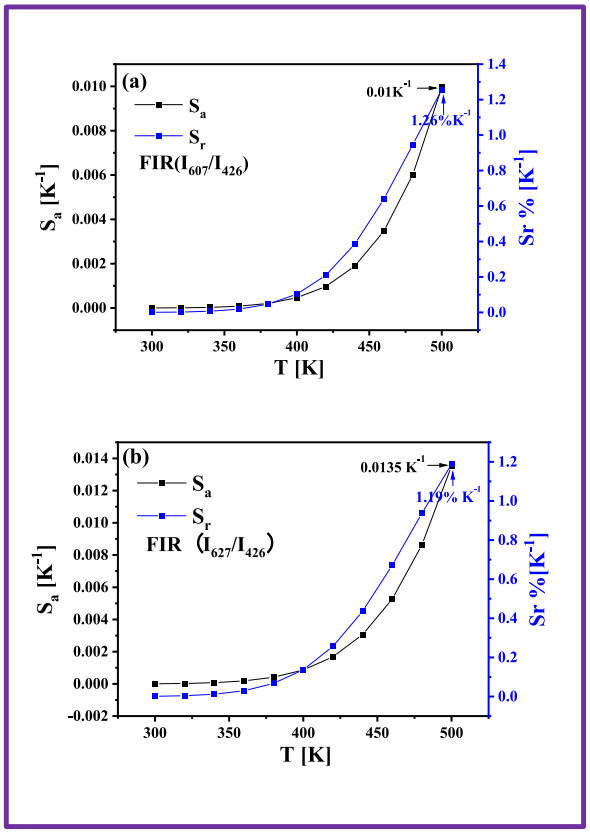

Fig. 11. The corresponding absolute sensitivity (S_a) and relative sensitivity (S_r) versus temperature for $FIR_{(I607/I426)}$ (a) and $FIR_{(I627/I426)}$ (b) as reference signals under excitation at 301 nm.

Table 1
Comparison with the sensitivity of some reported temperature sensing materials.

Compounds	Max. S_a (K^{-1})	Max. S_r (% K^{-1})	Temperature range (K)	Ref.
$Ca_2YZr_2Al_3O_{12}$: Bi^{3+}/Eu^{3+}	0.0082	0.66	297–573	[39]
$Ca_2Y_8(SiO_4)_6O_2$: Bi^{3+}, Eu^{3+}	0.0717	0.95	298–523	[4]
$Ca_3Sc_2Si_3O_{12}$: $Bi^{3+}/Tb^{3+}/Eu^{3+}$	0.094	1.0	300–500	[16]
$CaLaMgTaO_6$: Bi^{3+}/Eu^{3+}	0.0127	1.33	303–573	[18]
$LaNbO_4$: Bi^{3+}/Eu^{3+}	0.044	1.89	300–480	[14]
GdY_2SbO_7: Bi^{3+}, Eu^{3+}	0.01	1.26	300–500	This word

The ratio of fluorescence intensities at I_{607}/I_{426} and I_{627}/I_{426} were used as the reference values.

The absolute sensitivity (S_a) and relative sensitivity (S_r) can be expressed by following equations (4) and (5) [14]:

$$S_a = \left|\frac{\partial FIR}{\partial T}\right| \approx B\exp\left(-\frac{\Delta E}{k_B T}\right) \times \frac{\Delta E}{k_B T^2} \tag{4}$$

$$S_r = 100\% \times \left|\frac{1}{FIR}\frac{\partial FIR}{\partial T}\right| = 100\% \times \frac{B\exp\left(-\frac{\Delta E}{k_B T}\right)}{C + B\exp\left(-\frac{\Delta E}{k_B T}\right)} \times \frac{\Delta E}{k_B T^2}. \tag{5}$$

The calculated results are shown in Fig. 11 (a) and (b) for $FIR_{I607\ /I426}$ and $FIR_{I627\ /\ I426}$, from which it can be seen that both the S_a and S_r reach their maximum values of 0.01 K^{-1} and 1.26 % K^{-1} at 500 K when $I_{607/426}$ is used as the reference signal. When the reference signal is $I_{627/426}$, the maximum values of S_a and S_r are 0.0135 K^{-1} and 1.19 % K^{-1} at 500 K. Some materials reported for optical temperature measurement are shown in Table 1. Compared to the materials in Table 1, the phosphors developed herein demonstrate relatively outstanding performance.

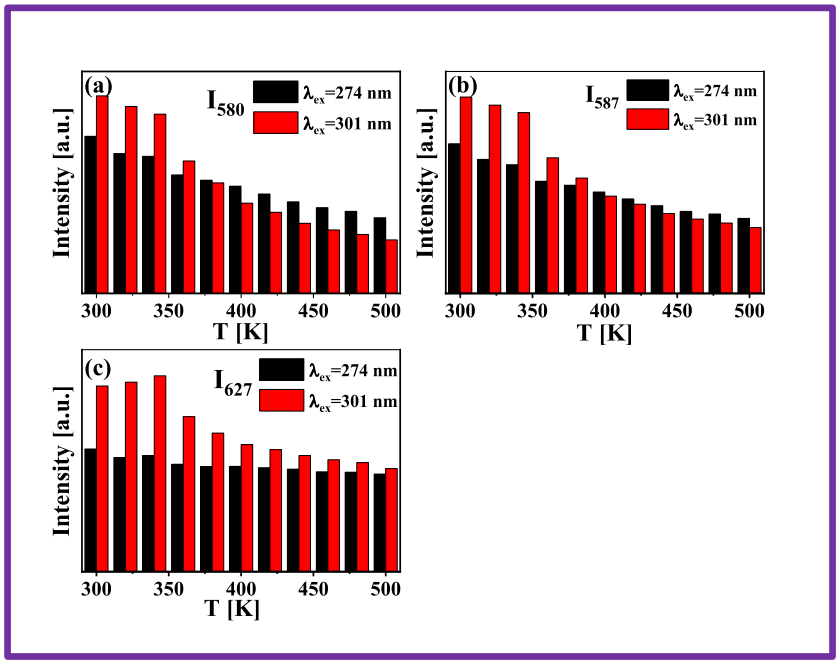

Fig. 12. Histograms of $I_{580(274/301)}$ (a), $I_{587(274/301)}$ (b), and $I_{627(274/301)}$ (c) with temperature for the double excitation method.

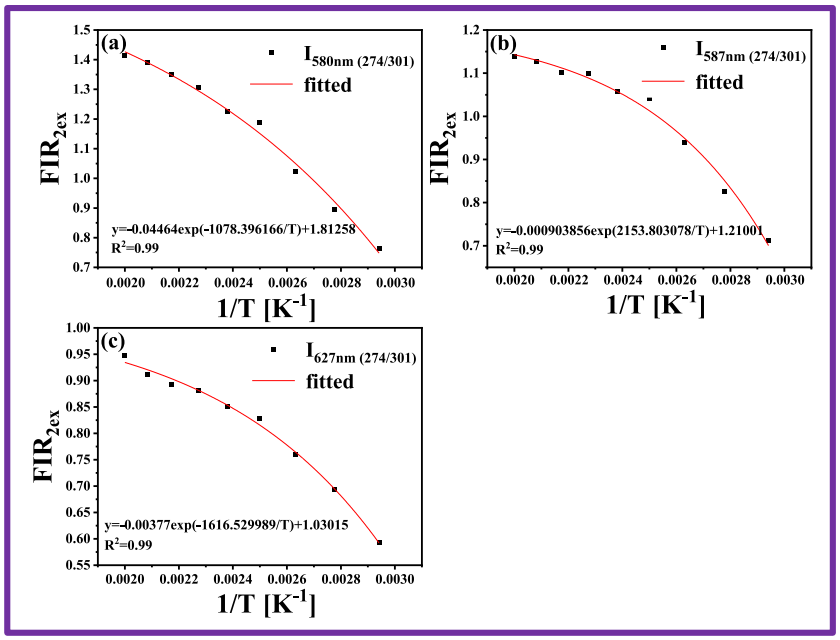

Fig. 13. Exponential fits in the double excitation mode (a), (b), (c).

In addition to the FIR-mode temperature measurement method, a double excitation method was considered [37]. The method is based on the fact that the Eu^{3+} to O^{2-} charge transfer band has a small energy gap (~3300 cm^{-1}) with the $^3P_1$ energy level of Bi^{3+}. The variation of fluorescence emission intensity with temperature was measured using 274 nm (CTB) and 301 nm ($^1S_0 \rightarrow {}^3P_1$) as excitation wavelengths, respectively. The selected emission positions were 580, 587, and 627 nm.

Fig. 12 (a)-(c) show the intensity histogram of the fluorescence emission intensity with temperature for emission position at 580, 587, and 627 nm, respectively, under different excitation conditions. It can be seen from the figure that the intensity of the emission peaks corresponding to the two excitation positions in the range of 340–500 K exhibits a notable tendency to decrease in different degrees. Therefore, an exponential function image of the fluorescence intensity ratio under the dual excitation conditions can be fitted

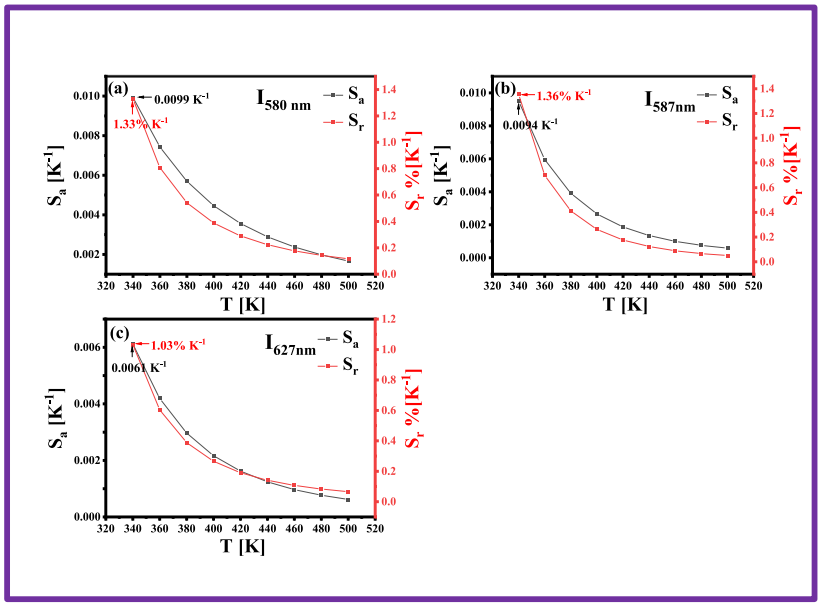

Fig. 14. The calculated results for S_a and S_r (a), (b), (c).

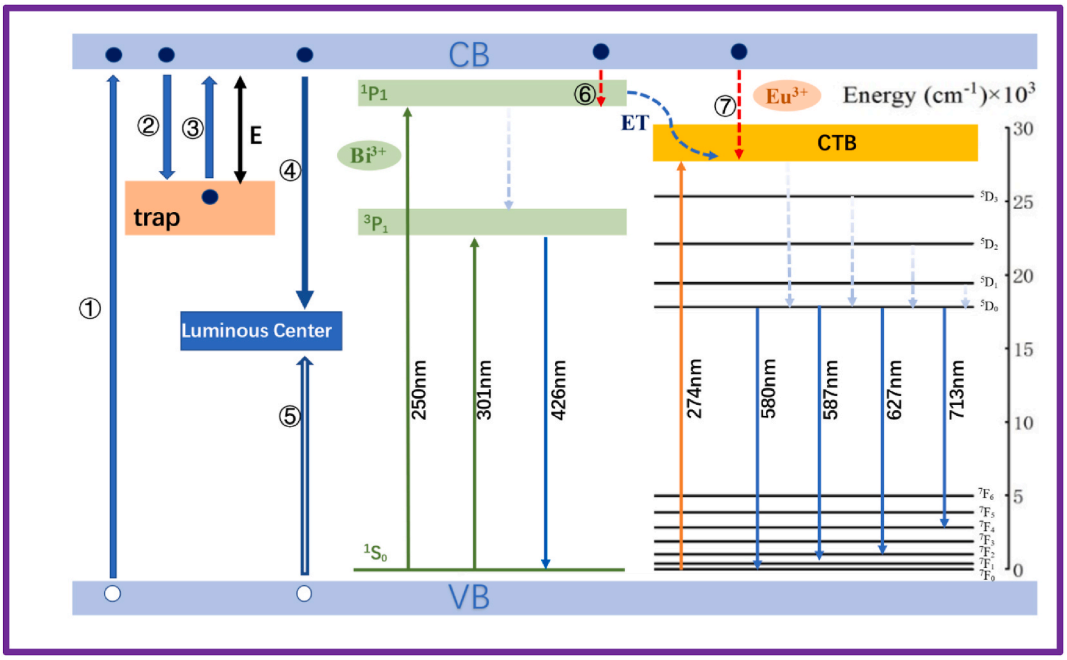

Fig. 15. The thermoluminescence schematic and the energy level diagrams of Bi^{3+} and Eu^{3+} in GYSO.

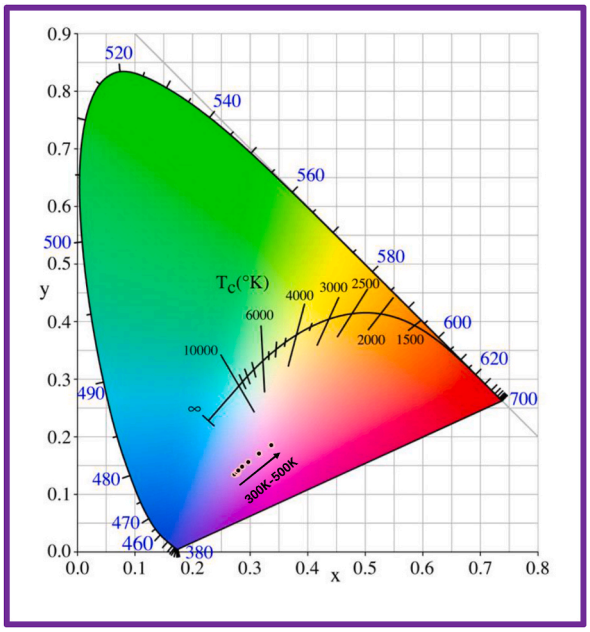

Fig. 16. CIE chromaticity diagram of GYSO:0.01Bi^{3+},0.05Eu^{3+}phosphor in the range of 300–500 K with 301 nm as the excitation wavelength.

accordingly, and the results are shown in Fig. 13 (a)-c).

The FIR_{2ex} fitting equation for the dual excitation mode is equation (6) [37]:

$$FIR^{2ex} = \frac{I_{274\text{nm}}(T)}{I_{301\text{nm}}(T)} = \frac{I_{274\text{nm}}}{I_{301\text{nm}}} \frac{1 + A_{274nm}\exp\left(-\frac{E_{274nm}}{k_B T}\right)}{1 + A_{301nm}\exp\left(-\frac{E_{274nm}}{k_B T}\right)} \approx C + B\exp\left(-\frac{\Delta E^{2ex}}{k_B T}\right), \tag{6}$$

where ΔE_{2ex} is the energy gap between the two thermally coupled energy levels, and the equation for S_a and S_r, in this case, can be expressed by equations (7) and (8) [37]:

$$S_a = \left|\frac{\partial FIR^{2ex}}{\partial T}\right| \approx B\exp\left(-\frac{\Delta E^{2ex}}{k_B T}\right) \times \frac{\Delta E^{2ex}}{k_B T^2} \tag{7}$$

$$S_r = 100\% \times \left|\frac{1}{\partial FIR^{2ex}}\frac{\partial FIR^{2ex}}{\partial T}\right| \approx 100\% \times \frac{B\exp\left(-\frac{\Delta E^{2ex}}{k_B T}\right)}{C + B\exp\left(-\frac{\Delta E^{2ex}}{k_B T}\right)} \times \frac{\Delta E^{2ex}}{k_B T^2}. \tag{8}$$

The results of the calculations are shown in Fig. 14 (a)-(c), where the maximum values of S_a and S_r are 0.0099 K^{-1} and 1.33 % K^{-1}, respectively, when $I_{580\ (274/301)}$ is selected as the reference signal. If $I_{587\ (274/301)}$ is selected as the monitoring signal, the maximum values of S_a and S_r are 0.0094 K^{-1} and 1.36 % K^{-1}, respectively. When $I_{627\ (274/301)}$ is chosen as the reference signal, the maximum values of S_a and S_r are 0.0061 K^{-1} and 1.03 % K^{-1}, respectively.

The thermoluminescence schematic and energy level diagram are shown in Fig. 15, which can fully explain the luminescence mechanism of the GYSO:Bi^{3+}, Eu^{3+} phosphors. As shown in Fig. 15, the excited electron jumps from the valence band to the conduction band (process ①) and generates an electron and a hole. Owing to the defects in the crystal structure of GYSO, the trap energy level is below the conduction band. The electrons that jump to the conduction band partly fall into the trap energy level (process ②). The rest of the electrons emit light, which is captured by the luminescence center (processes ④ and ⑤).

In the GYSO:Bi^{3+}, Eu^{3+} phosphors, the $^1P_1$ excited state of Bi^{3+} was very close to the $^5D_4$ energy levels of Eu^{3+}; therefore, it was easy to transfer the energy to the adjacent Eu^{3+} ions through resonance nonradiation. Afterward, Eu^{3+} ions transited from the ground state of $^7F_0$ to the excited state, relaxing to the $^5D_0$ level through the nonradiative path, and then returning to the ground state. The radiative transition to the ^7F_J (J = 0–4) levels produces red emissions from Eu^{3+} ions [4,38].

When the temperature rises, an increasing number of electrons in the trap energy level overcome the energy difference to leap to the conduction band (process ③) and produce fluorescence emission (processes ⑥ and ⑦). Hence, the fluorescence emission intensities of Bi^{3+} and Eu^{3+} do not decrease at 300–340 K, which is attributed to the compensation of the thermal burst by

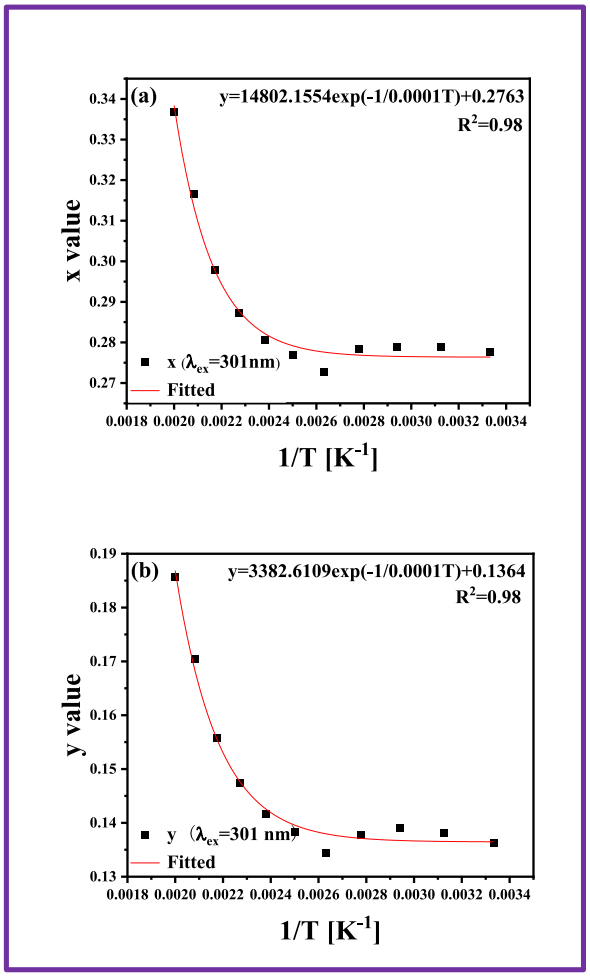

Fig. 17. The exponential fit plots with the x-value or y-value of the chromaticity coordinates as the reference signal under 301 nm excitation condition.

thermoluminescence.

To determine the variation of the chromaticity characteristics of the studied phosphors with temperature, the corresponding CIE chromaticity coordinates were calculated from the emission spectra of GYSO:0.01Bi^{3+}, 0.05Eu^{3+} in the range of 300–500 K and are shown in Fig. 16. When the temperature increased from 300 to 500 K under excitation of 301 nm, the chromaticity coordinates of the sample moved from (0.2776, 0.1363) to (0.3368, 0.1857). This phenomenon indicates the possibility of applying the studied sample to visual temperature measurements.

In addition, under the excitation of 301 nm, the change of the x and y values of the chromaticity coordinate with temperature is shown in Fig. 17 (a) and (b), rescpectively. As shown in the figure, with the x or y values as the ordinate coordinate and temperature as the abscissa, which can be well fitted to the exponential function, the values of S_a and S_r can be calculated using equations (2) and (3). The results are shown in Fig. 18 (a) and (b). When the excitation wavelength is 301 nm, the S_r of the sample reaches maximum values of 0.4539 % K^{-1} and 0.5996 % K^{-1} at 500 K when x and y values are used as reference signals, respectively. This implies that the change of chromaticity coordinates with temperature can also be a supplementary strategy for non-contact temperature measurement.

4. Conclusion

Novel GdY_2SbO_7:Bi^{3+}, Eu^{3+} phosphors with double emission were prepared using the high-temperature solid-phase method. The blue emission of Bi^{3+} ($^3P_1 \rightarrow {}^1S_0$) and the orange emission of Eu^{3+} ($^5D_0 \rightarrow {}^7F_{0,\ 1,\ 2,\ 3,\ \text{and}\ 4}$) occurred under excitation at 301 nm. The temperature dependence of the fluorescence emission intensity of the samples was tested in the range of 300–500 K. The S_a and S_r of the samples were calculated using FIR and thermochromic modes, respectively. The best mode for GdY_2SbO_7:Bi^{3+}, Eu^{3+} was the FIR based on double excitation method which S_r reached 1.36 % K^{-1} at 340 K. It indicates that GdY_2SbO_7:Bi^{3+}, Eu^{3+} phosphor exhibits potential applications in the field of optical temperature measurement.

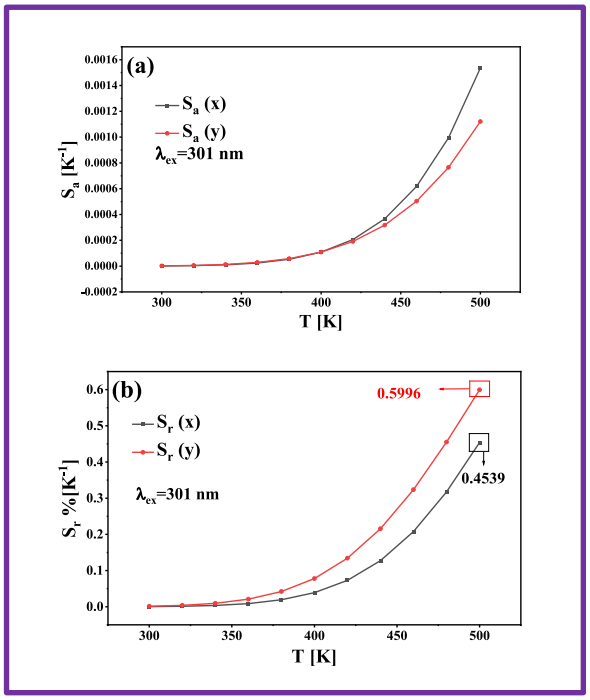

Fig. 18. The values of S_a and S_r with the x-value or y-value of the chromaticity coordinate as the reference signal under 301 nm excitation condition in the range of 300–500 K.

Additional information

No additional information is available for this paper.

Data availability statement

Data included in article/supplementary material/referenced in article.

CRediT authorship contribution statement

Yanru Yin: Writing – original draft. **Mengmeng Jiang:** Writing – original draft, Formal analysis, Data curation. **Lianhua Tian:** Writing – review & editing, Supervision, Resources, Investigation, Funding acquisition.

Declaration of competing interest

The authors declare that they have no known competing financial interests or personal relationships that could have appeared to influence the work reported in this paper.

References

[1] J.J. Qian, Z.J. Zhao, Q.M. Zhang, M. Werner, R. Petty, S. Abraham, M. Lu, Machine learning-assited optical thermometer for continuous temperature analysis inside molten metal, Sens. Actuators, A 322 (2021) 112626, https://doi.org/10.1016/j.sna.2021.112626.

[2] J. Qiao, X. Mu, L. Qi, Construction of fluorescent polymeric nano-thermometers for intracellular temperature imaging: a review, Biosens. Bioelectron. 85 (2016) 403–413, https://doi.org/10.1016/j.bios.2016.04.070.

[3] J.S. Liao, M.H. Wang, L.Y. Kong, J.H. Chen, X.Y. Wang, H.K. Yan, J.X. Huang, C.Y. Tu, Dual-mode optical temperature sensing behavior of double-perovskite $CaGdMgSbO_6$:Mn^{4+}/Sm^{3+} phosphors, J. Lumin. 226 (2020) 117492, https://doi.org/10.1016/j.jlumin.2020.117492.

[4] K. Li, R. Van Deun, Site-Bi^{3+} and Eu^{3+} dual emissions in color-tunable $Ca_2Y_8(SiO_4)_6O_2$:Bi^{3+}, Eu^{3+} phosphors prepared via sol-gel synthesis for potentially ratiometric temperature sensing, J. Alloys Compd. 787 (2019) 86–95, https://doi.org/10.1016/j.jallcom.2019.02.087.

[5] M. Vega, I.R. Martin, E. Cortés-Adasme, J. Llanos, Enhanced red up-conversion emission in Er^{3+}/Yb^{3+} co-doped $SrSnO^3$ for optical temperature sensing based on thermally and non-thermally coupled levels, J. Lumin. 244 (2022) 118687, https://doi.org/10.1016/j.jlumin.2021.118687.

[6] X.N. Yang, Q.H. Li, X. Li, B. Ma, Color tunable Dy^{3+} doped $Sr_9Ga(PO_4)_7$ phosphors for optical thermometric sensing materials, Opt. Mater. 107 (2020) 110133, https://doi.org/10.1016/j.optmat.2020.110133.

[7] Y. Gao, F. Huang, H. Lin, J. Xu, Y.S. Wang, Intervalence charge transfer state interfered Pr^{3+} luminescence: a novel strategy for high sensitive optical thermometry, Sensor Actuat B-Chem. 243 (2017) 137–143, https://doi.org/10.1016/j.snb.2016.11.143.

[8] P. Boutinaud, E. Pinel, M. Oubaha, R. Mahiou, E. Cavalli, M. Bettinelli, Making red emitting phosphors with Pr^{3+}, Opt. Mater. 28 (1–2) (2006) 9–13, https://doi.org/10.1016/j.optmat.2004.09.027.

[9] E. Glais, F. Massuyeau, R. Gautier, Tuning the emission color and temperature range of dual-mode luminescent thermometer by dopant valence states control, Appl. Mater. Today 26 (2022) 101349, https://doi.org/10.1016/j.apmt.2021.101349.

[10] F.W. Liu, D.G. Deng, M. Wu, B.W. Chen, L.Y. Zhou, S.Q. Xu, Alkali ions substitution induced tuning of sensitivity in mixed-valence europium ion co-doped $NaZr_2(PO_4)_3$ thermochromic phosphor for optical thermometry, J. Alloys Compd. 865 (2021) 158820, https://doi.org/10.1016/j.jallcom.2021.158820.

[11] S.W. Yuan, S. Zhao, L.L. Lou, D.Y. Zhu, Z.F. Mu, F.G. Wu, Fluorescence intensity ratio optical thermometer $YNbO_4$: Pr^{3+}, Tb^{3+} based on intervalence charge transfer, Powder Technol. 395 (2022) 83–92, https://doi.org/10.1016/j.powtec.2021.09.053.

[12] X.G. Zhang, Z.P. Zhu, Z.Y. Guo, Z.S. Sun, Y.B. Chen, A ratiometric optical thermometer with high sensitivity and superior signal discriminability based on $Na_3Sc_2P_3O_{12}$: Eu^{2+}, Mn^{2+} thermochromic phosphor, Chem. Eng. J. 356 (2019) 413–422, https://doi.org/10.1016/j.cej.2018.09.075.

[13] Z.H. Gao, F.Y. Fu, L.L. Niu, M. Jin, X.H. Wang, Emission-tunable Ba_2Y_{1-Sc} NbO_6:Bi^{3+} ($0 \le x \le 1.0$) phosphors for white LEDs, J. Rare Earths 40 (12) (2022) 1819–1826, https://doi.org/10.1016/j.jre.2021.08.021.

[14] J.P. Xue, Z.K. Yu, H.M. Noh, B.R. Lee, B.C. Choi, S.H. Park, J.H. Jeong, P. Du, M.J. Song, Designing multi-mode optical thermometers via the thermochromic LaNbO4:Bi^{3+}/Ln^{3+} (Ln = Eu, Tb, Dy, Sm) phosphors, Chem. Eng. J. 415 (2021) 128977, https://doi.org/10.1016/j.cej.2021.128977.

[15] E. Rai, R.S. Yadav, D. Kumar, A.K. Singh, V.J. Fulari, S.B. Rai, Influence of Bi^{3+} ion on structural, optical, dielectric and magnetic properties of Eu^{3+} doped $LaVO_4$ phosphor, Spectrochim. Acta 243 (2020) 118787, https://doi.org/10.1016/j.saa.2020.118787.

[16] Z. Sun, M.C. Jia, Y.L. Wei, J.C. Cheng, T.Q. Sheng, Z.L. Fu, Constructing new thermally coupled levels based on different emitting centers for high sensitive optical thermometer, Chem. Eng. J. 381 (2020) 122654, https://doi.org/10.1016/j.cej.2019.122654.

[17] J.W. Wang, R.S. Lei, S.L. Zhao, F.F. Huang, D.G. Deng, S.Q. Xu, H.P. Wang, Color tunable Bi^{3+}/Eu^{3+} co-doped La_2ZnTiO_6 double perovskite phosphor for dual-mode ratiometric optical thermometry, J. Alloys Compd. 881 (2021) 160601, https://doi.org/10.1016/j.jallcom.2021.160601.

[18] C.W. Xu, C.X. Li, D.G. Deng, H. Yu, L. Wang, C.Y. Shen, X.F. Jing, S.Q. Xu, Double perovskite structure $CaLaMgTaO_6$: Bi^{3+}, Eu^{3+} co-doped phosphors for optical temperature measurement, J. Lumin. 236 (2021) 118096, https://doi.org/10.1016/j.jlumin.2021.118096.

[19] Y.Y. Shen, Y. Chen, L. Chen, D.G. Deng, S.Q. Xu, Dual emitting from Bi^{3+}/Eu^{3+} co-activated $Sr_3La_2Ge_3O_{12}$ phosphor for optical thermometry, Opt. Mater. 115 (2021) 111036, https://doi.org/10.1016/j.optmat.2021.111036.

[20] J. Fu, F.W. Liu, L.Y. Zhou, R.G. Ye, D.G. Deng, S.Q. Xu, Dual-mode optical thermometry based on Bi^{3+}/Eu^{3+} co-activated $BaGd_2O_4$ phosphor with high sensitivity and signal discriminability, Ceram. Int. 47 (21) (2021) 30221–30233, https://doi.org/10.1016/j.ceramint.2021.07.202.

[21] X.S. Peng, J. Chen, Y.H. Chen, Y.C. Jiang, R.F. Wei, W.D. Zhou, H.J. Li, H. Guo, Optical thermometry based fluorescence intensity ratio in $Y2Mg_2Al_2Si_2O_{12}$:Bi^{3+}, Eu^{3+} phosphors, J. Alloys Compd. 885 (2021) 161010, https://doi.org/10.1016/j.jallcom.2021.161010.

[22] X. Liu, S.Q. Shi, K. Yang, L. Chen, D.G. Deng, S.Q. Xu, Temperature sensing characteristics of Bi^{3+}/Eu^{3+} co-activated $SrGa_2B_2O_7$: phosphor for dual-mode optical thermometry, J. Alloys Compd. 879 (2021) 160247, https://doi.org/10.1016/j.jallcom.2021.160247.

[23] H. Fan, Z.Z. Lu, Y.B. Meng, P.C. Chen, L.Y. Zhou, J.S. Zhao, X.T. He, Optical temperature sensor with superior sensitivity based on Ca_2LaSbO_6: Mn^{4+}, Eu^{3+} phosphor, Opt. Laser Technol. 148 (2022) 107804, https://doi.org/10.1016/j.optlastec.2021.107804.

[24] Y. Xie, X. Geng, Z. Hu, Z.J. Zhou, L. Zhou, Y.X. Zhao, J.X. Chen, W.S. Chen, N. Gong, B. Deng, R.J. Yu, Synthesis and photoluminescence properties of novel orange-emitting Sm^{3+}-activated $LaTiSbO_6$ phosphors for WLEDs, Opt. Laser Technol. 147 (2022) 107605, https://doi.org/10.1016/j.optlastec.2021.107605.

[25] H.J. Rossell, Fluorite-related phases Ln_3WO, Ln = rare earth, Y or SC, M = Nb, Sb, or Ta, J. Solid State Chem. 27 (1978) 115–122, https://doi.org/10.1016/0022-4596(79)90149-X.

[26] B.N. Tian, B.J. Chen, Y. Tian, X.P. Li, J.S. Zhang, J.S. Sun, H.Y. Zhong, L.H. Cheng, S.B. Fu, H. Zhong, Y.Z. Wang, X.Q. Zhang, H.P. Xia, R.N. Hua, Excitation pathway and temperature dependent luminescence in color tunable $Ba_5Gd_8Zn_4O_{21}$:Eu^{3+} phosphors, J. Mater. Chem. C 1 (12) (2013) 2338, https://doi.org/10.1039/c3tc00915g.

[27] S.A. Zhang, H.M. Luo, Z.F. Mu, J.M. Li, S.X. Guo, Z.Z. Li, Q. Wang, F.G. Wu, Photoluminescence and tunable emissions of $La_2(GeO_4)O$:Bi^{3+}, Eu^{3+} phosphor for ultraviolet converted light emitting diodes, J. Alloys Compd. 757 (2018) 423–433, https://doi.org/10.1016/j.jallcom.2018.05.066.

[28] S.A. Zhang, Y.H. Hu, L. Chen, X.J. Wang, G.F. Ju, Y. Fan, Photoluminescence properties of Ca_3WO_6:Eu^{3+} red phosphor, J. Lumin. 142 (2013) 116–121, https://doi.org/10.1016/j.jlumin.2013.03.058.

[29] S.J. Yoon, D.A. Hakeem, K. Park, Synthesis and photoluminescence properties of $MgAl_2O_4$:Eu^{3+} phosphors, Ceram. Int. 42 (1) (2016) 1261–1266, https://doi.org/10.1016/j.ceramint.2015.09.059.

[30] K. Park, J.W. Pi, D.A. Hakeem, Effect of alkaline metal ions on the photoluminescence properties of Eu^{3+}-doped $Ca_3Al_2O_6$ phosphors, J. Rare Earths 34 (12) (2016) 1193–1198, https://doi.org/10.1016/s1002-0721(16)60153-9.

[31] K.Y. Kim, S.J. Yoon, K. Park, Synthesis and photoluminescence properties of red-emitting $Ca_{3-3x/2}(VO_4)_2$:xEu^{3+} phosphors, J. Lumin. 160 (2015) 78–84, https://doi.org/10.1016/j.jlumin.2014.11.046.

[32] A. George, S.K. Jose, A. Jose, C. Joseph, P.R. Biju, Tunable multicolor luminescence and energy transfer mechanism in Eu^{3+}/Dy^{3+} co-doped $Ca_2Sb_2O_7$ phosphor under UV excitation, Opt. Laser Technol. 151 (2022) 108029, https://doi.org/10.1016/j.optlastec.2022.108029.

[33] E.L. Wang, K. Feng, J. Li, X.D. Zhou, X.K. Sun, Luminescence characteristics of $NaYGeO_4$:Bi^{3+}/Tb^{3+}/Eu^{3+} phosphors, J. Lumin. 250 (2022) 119108, https://doi.org/10.1016/j.jlumin.2022.119108.

[34] H.J. Jin, H. Wu, L.H. Tian, Improved luminescence of Y_2MoO_6:Eu^{3+} by doping Li^+ ions for light-emitting diode applications, J. Lumin. 132 (5) (2012) 1188–1191, https://doi.org/10.1016/j.jlumin.2011.12.066.

[35] R.S. Yadav, S.J. Dhoble, S.B. Rai, Enhanced photoluminescence in Tm^{3+}, Yb^{3+}, Mg^{2+} tri-doped ZnWO4 phosphor: three photon upconversion, laser induced optical heating and temperature sensing, Sensor Actuat B-Chem. 273 (2018) 1425–1434, https://doi.org/10.1016/j.snb.2018.07.049.

[36] B.H. Bai, G.J. Lu, C.Y. Cao, A. Umar, A.A. Ibrahim, N.H. Huang, Z.J. Chen, H.W. Zhao, W. Yao, H.C. Zhong, Y.C. Li, A. Xie, Temperature-induced luminescence enhancement and quenching behavior of Eu^{3+} in $Lu_2(WO_4)_3$ phosphors, Mater. Res. Bull. 169 (2024) 112502, https://doi.org/10.1016/j.materresbull.2023.112502.

[37] J. Periša, Z. Ristić, V. Đorđević, M. Sekulić, T. Dramićanin, Ž. Antić, M.D. Dramićanin, Multiparametric luminescence thermometry from Dy^{3+}, Cr^{3+} double activated YAG, J. Lumin. 238 (2021) 118306, https://doi.org/10.1016/j.jlumin.2021.118306.

[38] S.H. Fu, L.H. Tian, Red luminescence $Ca_{1-x}La_{2x/3}TiO_3$:Eu^{3+} phosphor with high quantum efficiency for ultraviolet-based white light-emitting diodes, J. Lumin. 216 (2019) 116715, https://doi.org/10.1016/j.jlumin.2019.116715.

[39] Z.G. Zheng, J.F. Zhang, X.Y. Liu, R.F. Wei, F.F. Hu, H. Guo, Luminescence and self-referenced optical temperature sensing performance in $Ca_2YZr_2Al_3O1_2$:Bi^{3+}, Eu^{3+} phosphors, Ceram. Int. 46 (5) (2020) 6154–6159, https://doi.org/10.1016/j.ceramint.2019.11.081.